

Raw Data Is All You Need: Virtual Axle Detector with Enhanced Receptive Field

Henrik Riedel^{a,*}, Steven Robert Lorenzen^a, Clemens Hübner^a

^a*Institute of Structural Mechanics and Design, Department of Civil and Environmental Engineering, Technical University of Darmstadt, Franziska-Braun-Str. 3, Darmstadt, 64287, Hessen, Germany*

Abstract

Rising maintenance costs of ageing infrastructure necessitate innovative monitoring techniques. This paper presents a new approach for axle detection, enabling real-time application of Bridge Weigh-In-Motion (BWIM) systems without dedicated axle detectors. The proposed method adapts the Virtual Axle Detector (VAD) model to handle raw acceleration data, which allows the receptive field to be increased. The proposed Virtual Axle Detector with Enhanced Receptive field (VADER) improves the F_1 score by 73% and spatial accuracy by 39%, while cutting computational and memory costs by 99% compared to the state-of-the-art VAD. VADER reaches a F_1 score of 99.4% and a spatial error of 4.13 cm when using a representative training set and functional sensors. We also introduce a novel receptive field (RF) rule for an object-size driven design of Convolutional Neural Network (CNN) architectures. Based on this rule, our results suggest that models using raw data could achieve better performance than those using spectrograms, offering a compelling reason to consider raw data as input.

Keywords: Sound Event Detection, Continuous Wavelet Transformation, Moving Load Localisation, Nothing-on-Road, Free-of-Axle-Detector, Bridge Weigh-In-Motion, Structural Health Monitoring, Field Validation

1. Introduction

As infrastructure ages, novel methods are imperative for efficient monitoring. Precise knowledge of the actual stress on infrastructure enables more accurate determination of remaining service life, identification of overloaded vehicles, and more efficient planning for new constructions. Weigh-In-Motion (WIM) systems offer a means to ascertain axle loads during regular traffic flow [1, 2, 3, 4, 5, 6]. Conventional WIM systems necessitate installation directly into roadways or tracks, often requiring traffic disruption. Conventional WIM systems are therefore expensive and hardly suitable for a nationwide investigation of axle loads. In contrast, Bridge WIM systems (BWIM) are positioned beneath bridge structures, facilitating reuse and repositioning for multiple BWIM measurements [7, 8, 9, 10]. Thus, the installation of a BWIM system is less expensive and can be

used for a multitude of time-limited investigations. For large-scale investigations of axle loads, BWIM systems are therefore hardly dispensable. However, effective utilization of BWIM systems typically demands knowledge of axle load positioning [10, 11, 12]. For this purpose, additional sensors currently need to be installed at specific locations (facing the roadway, on the cross girders, or near the supports) that depend on the bridge structure [13, 14, 15, 16]. Only in the case of thin slab bridges can BWIM strain sensors be reliably used for axle detection [17]. However, for a large scale application of BWIM measurements, a method for axle localization that is independent of bridge type and sensor position would be of great benefit, effectively reducing cost and risk.

Therefore, our study aims at an axle detection method using existing sensors of arbitrary BWIM systems. To determine the axle positions, axles are usually detected at at least two locations. With the distance between the locations and the difference in time, the axle position can then be interpolated or

*Corresponding author. E-mail address: riedel@ismd.tu-darmstadt.de (H.Riedel).

extrapolated for any point in time. Detecting events in time series the term Sound Event Detection (SED) predominates in literature [18, 19, 20, 21]. One of the tasks of SED is for example speech recognition. Here, events refer to words and audible sound is used as input. However, this methodology can also be applied to other vibration signals as input (such as accelerations in bridges) and other events (such as a train axle passing a bridge). For SED problems, time series are typically analyzed in the form of 2D spectrograms using Convolutional Neural Networks (CNNs) [22, 23] or, more recently, Transformers [24], despite the competitive performance of 1D CNNs [25]. Consequently, research often concentrates on identifying the most suitable spectrogram type [26, 27]. Notably, in conventional tasks like speech recognition and acoustic scene classification, log mel spectrograms dominate [19, 28, 24], despite some studies showing better or comparable outcomes using raw data [26, 29, 30, 31]. In the context of axle localization, Continuous Wavelet Transformations (CWTs) have demonstrated suitability as features for axle detection [32, 33, 34, 12, 35, 36]. Given that CWTs even compete well in speech recognition [26] and log mel spectrograms were tailored for human auditory perception, CWTs were adopted in our earlier work for axle detection [36]. However, it is unclear whether CWTs are actually necessary, whether raw measurement data is sufficient as model input, and how this affects the model's performance.

In this study, we propose an novel approach capable of real-time axle detection (e.g. x axles were detected) and axle localization (e.g. an axle was located at time y at location z) using sensors placed arbitrarily. Consequently, BWIM systems can now conduct real-time axle detection without the need for additional sensors. To validate our approach, we adapted the VAD model [36] to handle raw measurement data and performed several tests on the dataset from Lorenzen et al. [37].

2. Methodology

In this section, we outline the methodology used for the Virtual Axle Detector with Enhanced Receptive field (VADER) in comparison to the predecessor model Virtual Axle Detector

(VAD). The data set from Lorenzen et al. [37] is briefly summarized. Finally, the training parameters and evaluation metrics are described.

2.1. Data Acquisition

The dataset from Lorenzen et al. [37] was acquired on a single-span steel trough railway bridge situated on a long-distance traffic line in Germany (fig. 1). This bridge is 18.4 meters long with a free span of 16.4 meters and a natural frequency of about 6.9 Hz for the first bending mode. The natural frequency is variable with a non-linear dependence on the load. Measurement data from ten seismic uniaxial accelerometers with a sample rate of 600 Hz installed along the bridge are used as features.

Utilizing a supervised learning approach, our model requires labels as the ground truth from which to learn. For the creation of the labels, four rosette strain gauges were used to ensure that the accuracy is sufficient to evaluate the model. The rosette strain gauges were used to determine the axle positions and velocities which were then interpolated or extrapolated for the positions of the accelerometers [36]. So that strain gauge measurements are not necessary for the application, two scenarios for labeling are investigated in this study: existing data from a failed axle detector and trains with a differential global positioning system (DGPS). The dataset consist out of 3,745 train passages with one label vector per sensor. The label vector contains ones at the time points when a train axle is positioned above the respective sensor, and the rest are zeros (fig. 2). Therefore, the sum of the label vector yields the number of axles of the corresponding train. The model then only receives the acceleration signals of a single sensor at a time and predicts the times at which an axle is located above this sensor. From a number of 2 acceleration sensors, the axle distances and velocities can thus also be determined. Due to the sampling rate, an inaccuracy of 6-38 cm is assumed for the label creation, depending on the train's velocity and the sensor's position. For more detailed information, please refer to the paper by Lorenzen et al. [36].

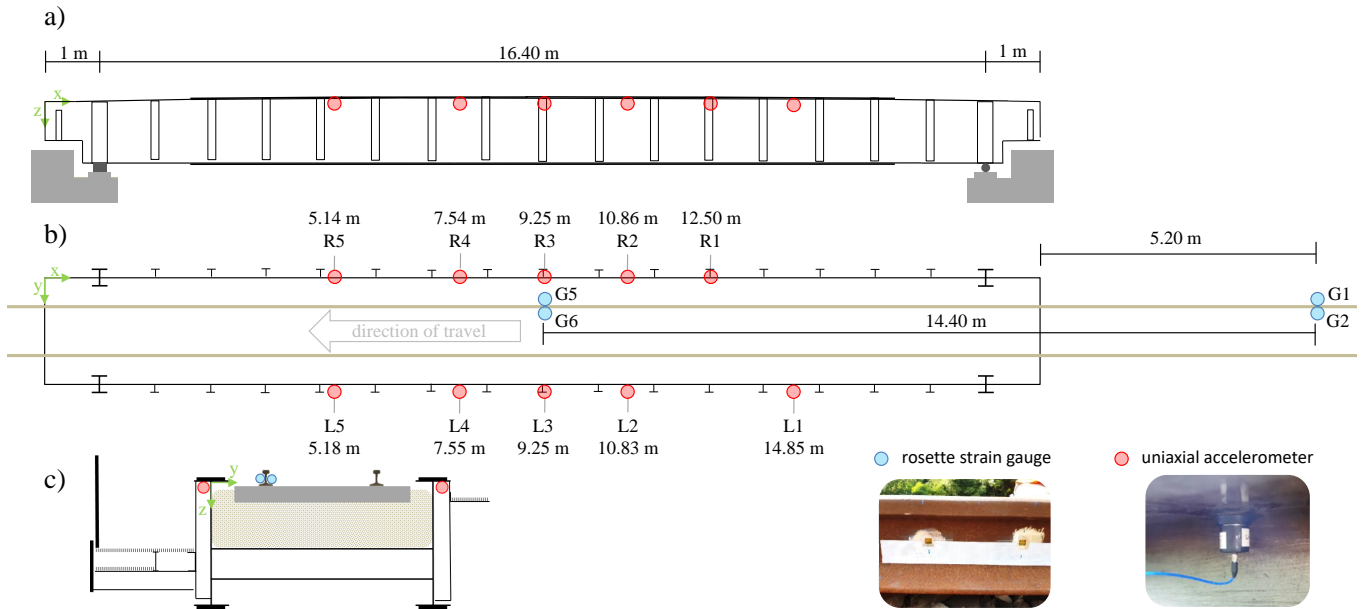


Figure 1: Bridge and sensor setup a) side view b) top view with sensor labels, accelerometers x -ordinate and strain gauge distances c) cross section. [37]

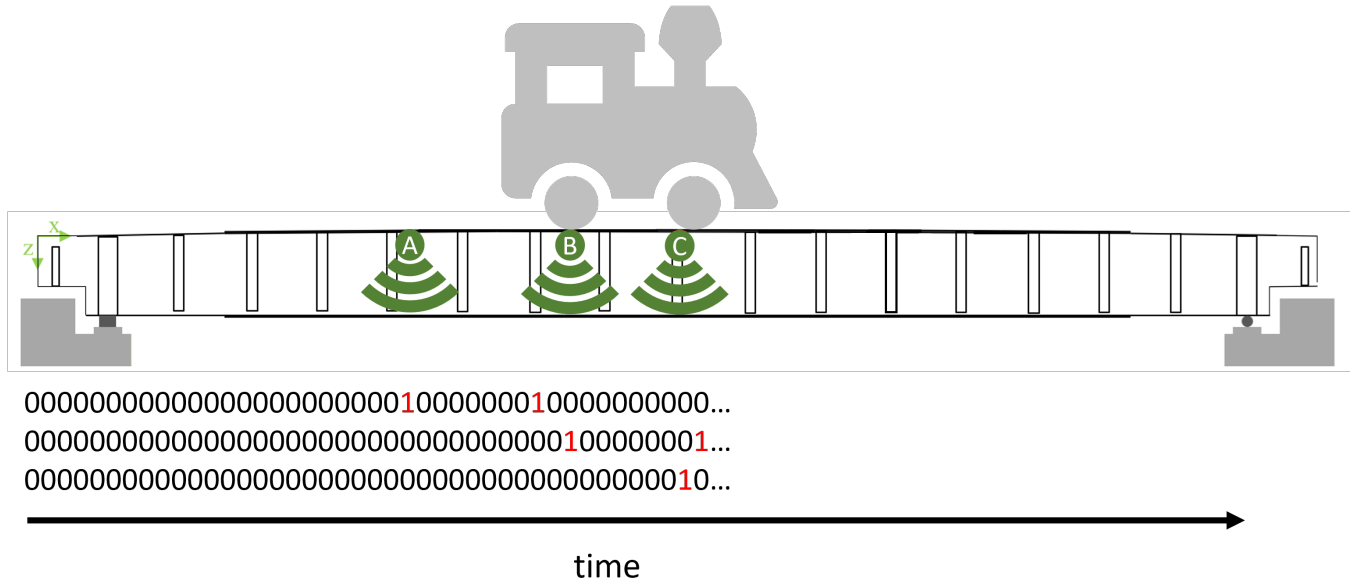


Figure 2: The labels represent the moment when a train axle is located over the respective sensor. Here, as an example, potential label vectors are shown for three fictitious sensors and a train up to the time shown. Derived from Lorenzen et al. [36].

2.2. Data Transformation

The VAD model uses CWTs as features with three mother wavelets and two sets of 16 frequencies per mother wavelet [36]. This results in an input tensor of $16 \times 6 \times n_s$ with n_s for number of samples in the acceleration signal of a sensor. The proposed VADER model is optimized for raw acceleration signals without any preprocessing. Therefore VAD operates in the frequency-time domain while VADER operates in time domain.

2.3. Data Split

The training and validation sets were implemented using a five-fold cross-validation approach with a holdout test set. Initially, one-sixth of the data was separated for the test set. The remaining data was divided into five folds. During training, a different fold was used as the validation set in each iteration, while the other four folds were used for training. Training concluded based on the validation set results, and the model was consistently tested on the same test set. This process allowed the model to be evaluated five times using the same data, providing a more accurate estimation of its generalization capability [38].

To further investigate the applicability of the proposed concept, the dataset was divided into folds based on the number of train axles in two different ways. In the first split, the model is intended to function as a surrogate for a malfunctioning axle detector. For this purpose, the data set was split for all folds and the test set in a **stratified** fashion (fig. 3a), resulting in 3,110 passages with 112,038 individual axles for training and 623 passages with 22,472 individual axles for testing. In the second split, the model was provided only with axle positions from a specific train type equipped with a differential global positioning system (**DGPS**). Since the exact construction series of the trains for determining the train types are not known, the train length in axles was used as a simplified criterion instead. Trains with the most frequent axle count were used for the five-fold cross-validation sets, while all other train lengths were included in the test set (fig. 3b). This results in 1,916 passages with 61,312 individual axles for training and 1,817 pas-

sages with 73,198 individual axles for testing. With the stratified splits, training is done with about 5/6 of the data and testing with 1/6 of the data, whereas the splits in the DGPS set for training and testing are about the same size. Thus, in the case of DGPS splits, in addition to having significantly less data available for training, these data are also not representative of all trains. It should be noted that with non-representative data sets, inadequate results are usually to be expected [38]. Thus, the DPGS splits are suitable for testing the models under particularly difficult conditions.

2.4. Model Definition

The VADER model is a modification of the VAD model designed for one-dimensional instead of two-dimensional inputs with some minor adjustments to the state-of-the-art. VAD and VADER were implemented as a fully convolutional neural networks (FCNs) [39] to handle inputs of arbitrary lengths. This property is particularly advantageous for the detection of train axles, as the crossing time varies significantly based on the train's speed and the number of axles.

The U-Net concept [40] was chosen for the model architecture, originally developed for semantic segmentation of images, but also adaptable for segmenting time series data. The fundamental concept of the U-Net architecture is the encoder path and the decoder path. In the encoder path, the resolution is progressively reduced and information is compressed, while in the decoder path, the resolution is increased back to the original dimensions (fig. 4). The encoder path aims to capture details at various resolutions, while the decoder path integrates these details into the appropriate context. The intermediate results from the encoder and decoder paths at the same resolution are combined through skip connections.

Our implementation of the U-Net comprises of a well established combination of convolution blocks (CBs), residual blocks (RBs) [41], max pooling layers, concatenate layers, and transposed convolution layers (fig. 4, 5). A CB always consists of a convolution layer with ReLU activation and a normalization layer. For the VAD model, batch normalization [42]

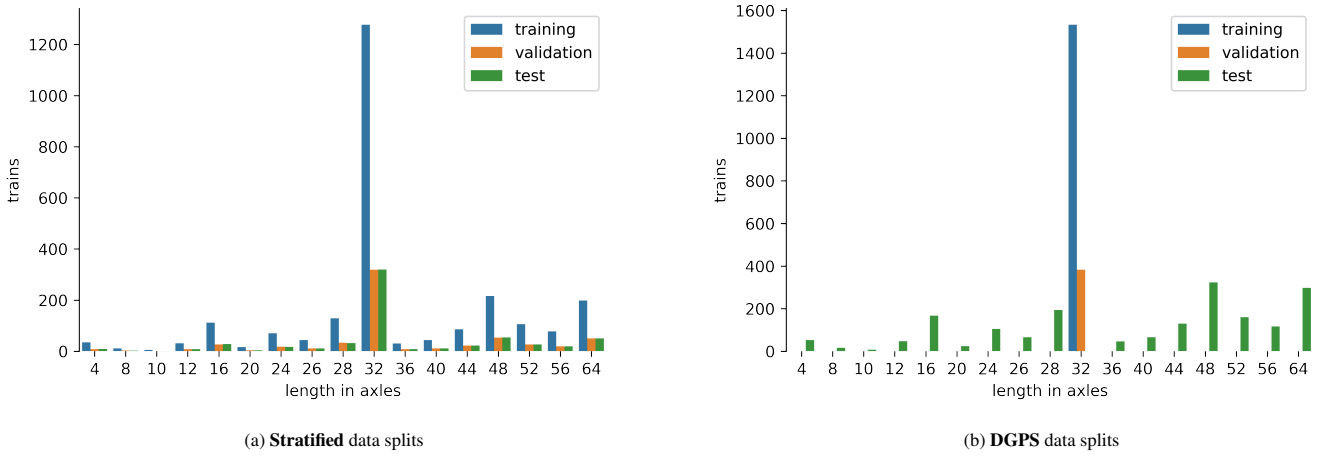


Figure 3: Train lengths defined by number of axles in both splits for the first combination of folds of a five-fold cross-validation.

was chosen, and for the VADER model, the more recent group normalization [43] with 16 channels per group was employed. Group normalization was shown to be less sensitive to other parameters like batch size and was therefore chosen to effectively reduce the hyperparameter space. The RBs were implemented similarly to the 50-layer or larger variants of the ResNet [41]. The final layer in both models is a convolution layer with only one filter and sigmoid activation. In VADER, the first group normalization layer has only one group, making it functionally similar to layer normalization [43]. Additionally, a gaussian noise (GN) with a noise standard deviation of 0.5 was added after the first layer, aiming to aid in the model’s generalization-ability.

The VAD model (fig. 4) uses the default kernel size of 3×3 and the default pooling size of 2 for 2D inputs [38]. This halves the temporal resolution with each pooling step. In the bottleneck layers, the temporal resolution is reduced by a factor of 16, giving the model a receptive field of $16 \times 3 = 48$ with a kernel size of 3. Thus, the model can examine at least 48 samples at the same time.

The bridge has a natural frequency of 6.9 Hz (depending on the load), and to distinguish the contribution of the bridge from the axle loads’ structural response, a receptive field of at least $\frac{600 \text{ Hz}}{6.9 \text{ Hz}} \approx 87$ samples would be necessary. Through the CWT transformation, information about frequencies up to approxi-

mately 3.4 Hz has been encapsulated into individual sample values. Therefore, the CWT transformation can effectively increase the receptive field to $\frac{600 \text{ Hz}}{3.4 \text{ Hz}} \approx 176$ samples.

Since the VADER model (fig. 5) processes only 1D data, the same number of parameters are required for a kernel size of 9×1 as for the kernel size of 3×3 in the VAD model. As the kernel size is larger, the pooling size can also be increased. The pooling size was chosen such that the receptive field and hence the kernels can cover a frequency of 1 Hz. Therefore, we propose the receptive field (RF) rule to calculate the required size of the largest receptive field in order to capture the lowest frequency of interest

$$y \geq \frac{f_s}{f_l}, \quad (1)$$

with f_s as sample frequency, f_l as lowest frequency of interest and y as the necessary size of the models largest receptive field in samples. Hence, to cover signals of 1 Hz at a sampling rate of 600 Hz, the receptive field must span at least 600 samples (eq. 1). With a pooling size of 3, this results in a receptive field of $3^4 \times 9 = 729$ samples. Therefore, in the case of VADER, the actual receptive field is over 15 times larger and the effective receptive field is over 4 times larger than that of VAD, while using the same number of parameters.

For the VADER model, we were able to double the number of RBs, while doing so with the VAD model led to overfitting

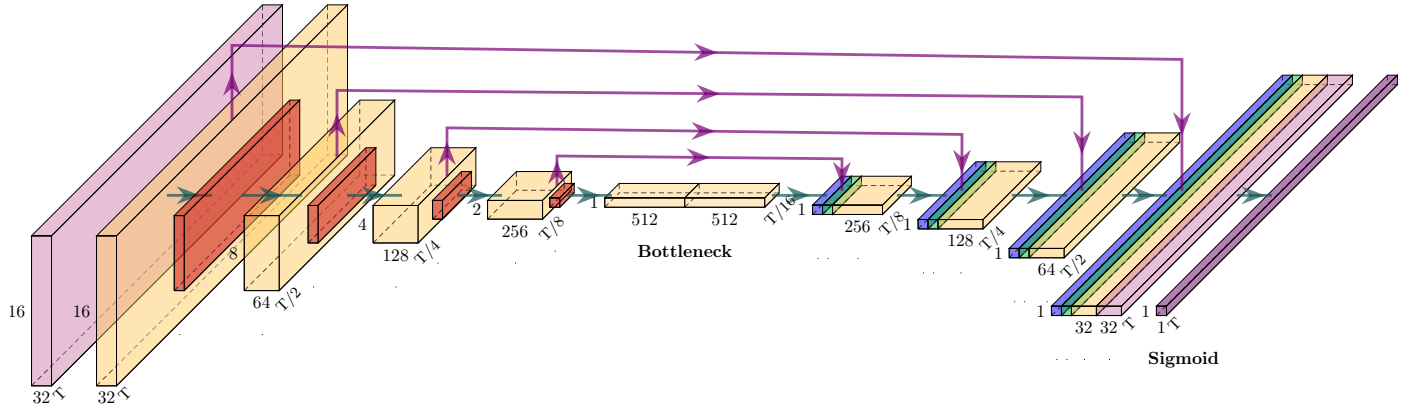


Figure 4: Definition of the Virtual Axle Detection model (VAD) with colored boxes corresponding to the following layers: CB (light purple), RB (yellow), max pooling (red), concatenate (green), transposed convolution (blue) and reshaping skip connection (purple arrow). Dimension of the feature maps at the corresponding boxes with T samples at the bottom right, feature maps at the bottom and frequencies at the left.

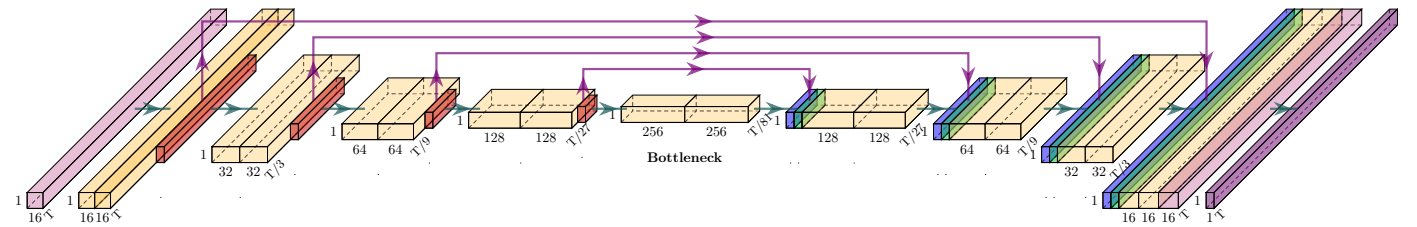


Figure 5: Definition of the Virtual Axle Detection with Enhanced Receptive field model (VADER) with colored boxes corresponding to the following layers: CB (light purple), RB (yellow), max pooling (red), concatenate (green), transposed convolution (blue) and reshaping skip connection (purple arrow). Dimension of the feature maps at the corresponding boxes with T samples at the bottom right, feature maps at the bottom and frequencies at the left.

and worse results. As a result, the VADER model has approximately twice as many learnable parameters as the VAD model overall.

The TensorFlow library [44] was used for implementation of the model and PlotNeuralNet [45] was used for visualising it.

2.5. Training Parameter

For the loss function, binary focal loss was chosen with an optimized γ value of 2.5 [36]. To evaluate the model's performance, the F_1 score (eq. 2) was used as the standard metric for imbalanced data sets [38]:

$$F_1 = 2 \times \frac{\text{precision} \times \text{recall}}{\text{precision} + \text{recall}} \quad (2)$$

where,

$$\text{precision} = \frac{\text{TruePositives}}{\text{TruePositives} + \text{FalsePositives}} \quad (3)$$

$$\text{recall} = \frac{\text{TruePositives}}{\text{TruePositives} + \text{FalseNegatives}} \quad (4)$$

To determine when an axle is considered correctly detected (*TruePositive*), two spatial threshold values were defined. The first threshold of 200 cm corresponds to the minimum assumed distance between two axles, and the second threshold of 37 cm corresponds to the maximum expected error in label creation. Training was conducted for an arbitrary maximum of 300 epochs with unchanged batch size of 16 [36]. Within an epoch, all training data is iterated through once. The adam optimization algorithm originally proposed by Kingma and Ba [46] with the default initial learning rate of 0.001. After two epochs without improvement in the F_1 score on the validation set, the learning rate was reduced by a factor of 0.3 (the default factor of 0.1 slowed down training to much), and the training was terminated after four epochs without improvement.

3. Results and Discussion

Training and validation results: Generally using raw data instead of CWTs is a significant reduction in computation time and memory requirements. For the 6 CWTs with 16

scales each as proposed in Lorenzen et al. [36], a 12-second traversal requires 1.4 seconds and about 5.7 MB of memory just for the transformation. In contrast, our approach takes only 0.022 seconds from raw data to prediction with about 61.1 KB memory usage. Therefore, when using raw data, inference becomes at least 65 times faster, while using only about 1 % of the memory for the input. In our case with 10 sensors the axle detection for a train with 64 axles would take $1.4 \text{ s} \times 10 \text{ sensors} \times 64 \text{ axles} = 896 \text{ s} \approx 5 \text{ min}$ with VAD and $0.022 \times 10 \text{ sensors} \times 64 \text{ axles} = 14,08 \text{ s}$ with VADER. Even for more realistic scenarios with e.g. 3 sensors VAD would still need minutes while VADER takes seconds to detect the axles and this does not even include the other side of the bridge, additional tracks and reduced computing power for on-site evaluation. With potentially trains a few minutes apart, the higher efficiency of VADER is thus needed for real-world application.

To compare the two models as effectively as possible, an initial investigation was conducted to determine whether GN could also aid the generalization capability of the VAD model. Contrary to expectations, the model's performance actually decreased with the addition of GN, and as a result, it was not further considered in subsequent analyses (fig. 6).

In the case of the DGPS split, the VAD model achieves a similar F_1 score on the training set as VADER. However, it can be observed that at the validation set, the VAD model starts to overfit around the third epoch (fig. 7a). In contrast, the VADER model initially achieves better results on the validation set, and it is only around the 15th epoch that the F_1 score on the training set becomes higher. Since the two curves are very close to each other, overfitting is not usually considered to be occurring at this point.

Based on the loss, it becomes even more evident that the VAD model starts overfitting around the 6th epoch, as the validation loss begins to rise to a value similar to that of the initial epochs (fig. 7b). In the case of the VADER model, there is also an indication of a tendency towards overfitting, although the validation loss remains at a low level and increases only slightly above its minimum.

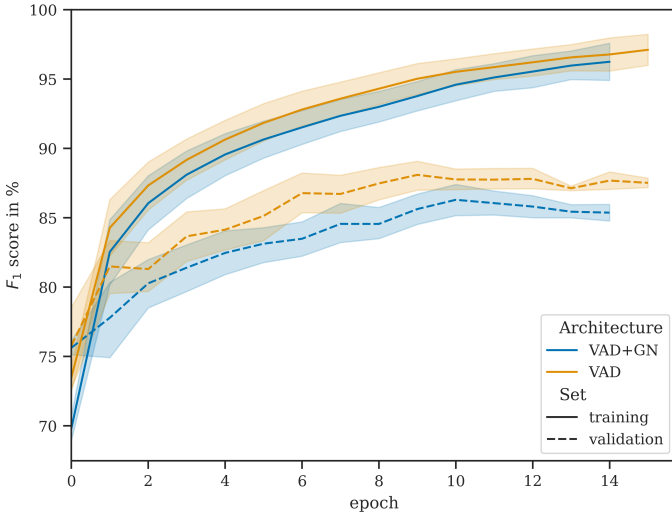


Figure 6: Comparison of the impact of GN as data augmentation on VAD model performance. F_1 scores for training and validation data sets with a single train length with confidence interval determined over the five folds.

For the VAD model, the F_1 score (fig. 7a) and the loss (fig. 7b) develop relatively similar to each other. In contrast, for the VADER model, the F_1 score improves monotonically until it converges, while the loss starts to deteriorate after about half of the epochs. In this context, the loss can be seen as a measure of model bias since it is calculated on a per-sample basis, counting only exact matches (no spatial error). This makes the loss sensitive to minor deviations from the label. On the other hand, the F_1 score can be regarded as a measure of model bias as it is calculated for each event (in this case, train axle) and allows for a certain spatial error (SE). For the SE, the temporal error is calculated first. The temporal error is the number of samples by which the prediction deviates from the label. With the axle speed, the temporal error is then converted into the SE. The F_1 score is a good descriptor of the model’s overall performance. Thus, the bias hardly decreases after the halfway point of training, while the variance increases. This suggests that the model is overfitting and training should be terminated earlier. However, as the increase in variance is only marginal, its influence on this investigation is considered minor.

In the stratified split, the difference between the two models becomes more pronounced. In terms of the F_1 score, the VAD model fails to achieve comparable results even on the training

data in comparison to the VADER model (fig. 7c) and is therefore underfitting. The training for both models is terminated approximately 10 epochs later than in the DGPS split. This suggests that due to the greater diversity of training data, the models overfit later and/or to a lesser extent. In the VAD model, the overfitting is less pronounced in terms of loss (fig. 7d), and the F_1 score exhibits a nearly convergent trend (fig. 7c). For the VADER model, the loss demonstrates a more noticeable increase and overfitting, which could also be attributed to the logarithmic scaling of the figure (fig. 7d). The F_1 score of the VADER model follows a similar trend for both splits (fig. 7c and 7a), indicating a lack of significant overfitting.

Test results: For the test results of the models, the learned parameters from the epoch with the best F_1 score on the validation set were chosen. Using these parameters, the models were then evaluated on the previously unseen test set. This procedure was repeated for all folds, so that both models (VADER and VAD) made predictions for both threshold values (200 cm and 37 cm) and both splits (stratified and DGPS).

The VADER model achieves significantly higher accuracy for both threshold values (200 cm and 37 cm) and both splits (stratified and DGPS) (fig. 8a, 8b). In general, it can be observed that the accuracy of both models is considerably better for the stratified split compared to the DGPS split. In the stratified split, the VADER model achieves such strong results that even the 25th percentile attains an F_1 score of 100 %. Notably, for the 200 cm threshold (fig. 8a), VADER attains a comparable accuracy with the more challenging split (DGPS), as VAD does with the simpler split (stratified). However, this observation is not consistent for the 37 cm threshold (fig. 8b).

For each threshold, split and metric, the average (avg) and standard deviation (SD) were calculated for all samples of the corresponding 5 folds. To better assess the risk of using VAD and VADER, the error reduction (ER) was calculated (right column in tab. 1):

$$ER = 100 \% - \frac{E_{\text{VADER}}}{E_{\text{VAD}}} \times 100 \% \quad (5)$$

where,

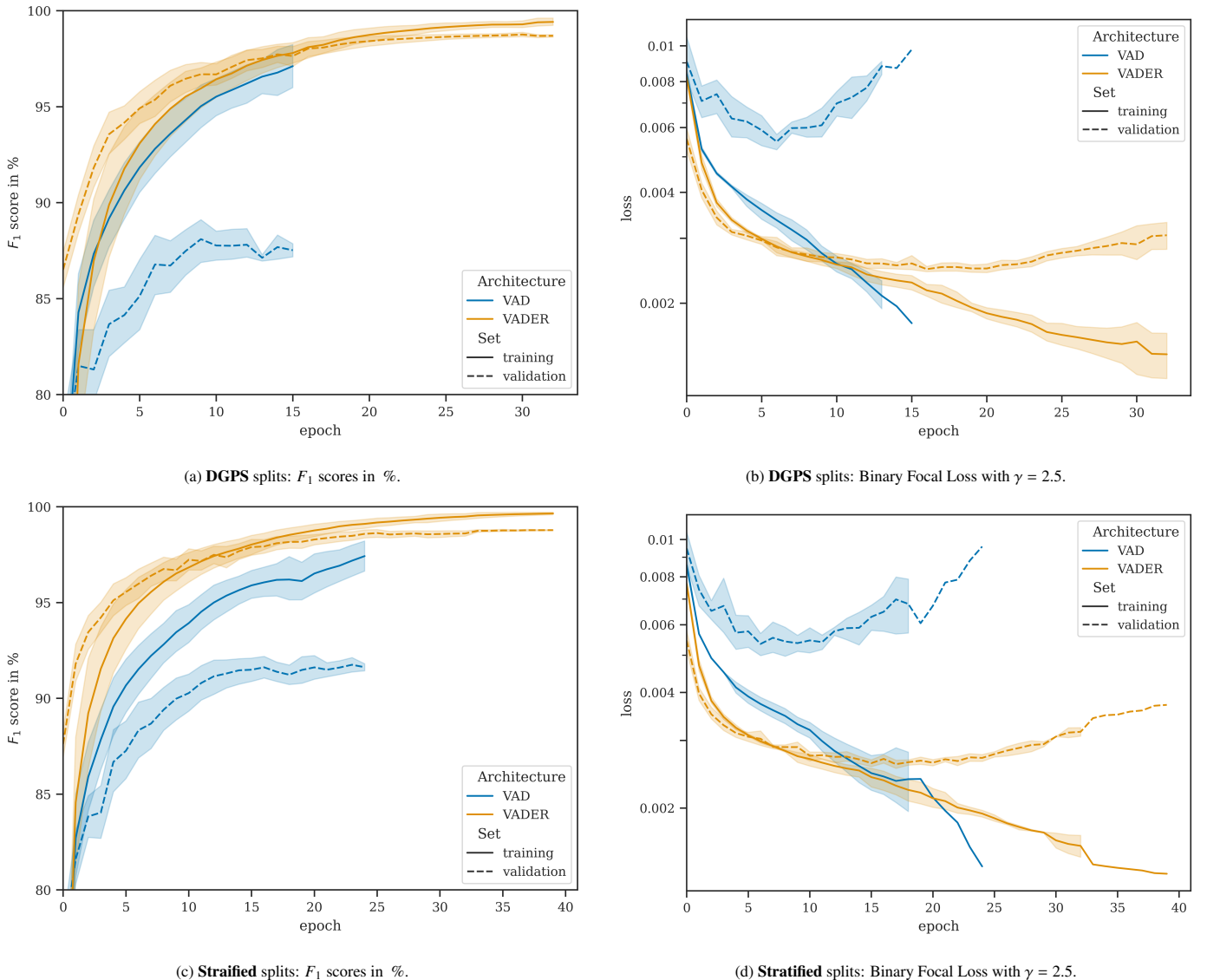
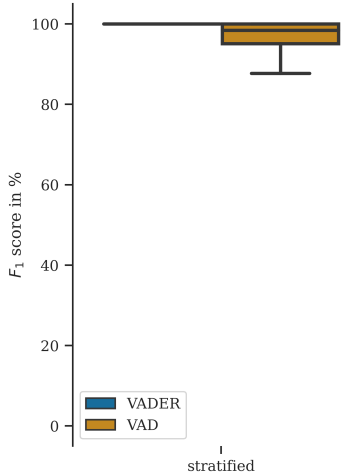
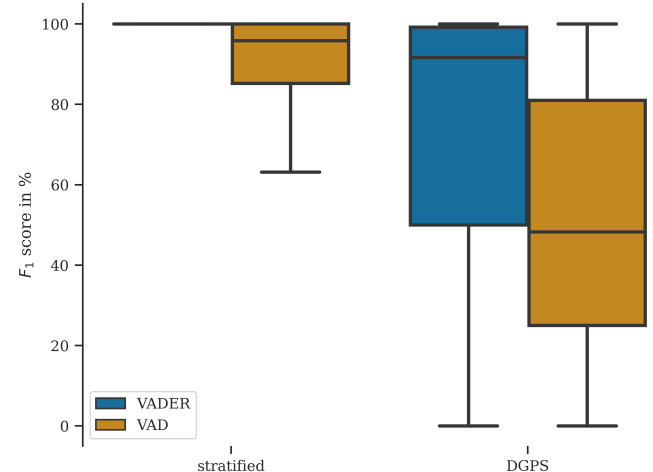


Figure 7: Results on training and validation sets per epoch with a single train length with confidence interval determined over the five folds.



(a) Threshold of 200 cm.



(b) Threshold of 37 cm.

Figure 8: F_1 score of the models for the two types of data split on the test sets. One data point was calculated per sensor, train and fold for a given threshold.

$$E_{\text{model}} = \begin{cases} 100 \% - F_1, & \text{for } F_1 \\ SE, & \text{for } SE \end{cases} \quad (6)$$

In 31 out of 32 cases, VADER performs better than VAD (tab. 1). VAD only performs better in the SD of the F_1 score with a threshold value of 37 cm and the stratified dataset. However, the error rate (eq. 5) of VADER compared to VAD is reduced on average by:

$$100 \% - \frac{100 \% - 95.7 \%}{100 \% - 88.3 \%} \times 100 \% = 63 \%$$

This means that the better SD of the F_1 score indicates that the VAD model is consistently significantly worse than the VADER model.

On average for all splits and thresholds, VADER reduced the error rate by 64.82 % while also reducing the SE by 37.59 % in comparison to VAD.

Sensor dependent test results: In the work by Lorenzen et al. [36], it was observed that one of the sensors was degraded. To investigate the influence of sensor degradation for each model and split more closely, the F_1 score for both threshold values and both splits (fig. 9a- 9d), and the spatial accuracy for both splits with a threshold value of 200 cm (fig. 9e- 9f) were examined per sensor. The spatial error was converted into

Threshold	Split	Metric	VAD	VADER	ER
37 cm	stratified	F_1 avg	88.3 %	95.7 %	63 %
		F_1 SD	0.17 %	0.31 %	-85 %
		SE avg	4.22 cm	3.11 cm	26 %
	DGPS	SE SD	7.05 cm	5.46 cm	23 %
		F_1 avg	55.7 %	79.4 %	53 %
		F_1 SD	1.21 %	0.45 %	62 %
200 cm	stratified	F_1 avg	95.4 %	98.5 %	68 %
		F_1 SD	0.27 %	0.15 %	44 %
		SE avg	11.3 cm	5.45 cm	52 %
	DGPS	SE SD	30.8 cm	16.7 cm	46 %
		F_1 avg	81.3 %	95.3 %	75 %
		F_1 SD	1.25 %	0.25 %	80 %
		SE avg	36.6 cm	19.7 cm	46 %
		SE SD	61.2 cm	41.8 cm	32 %

Table 1: F_1 score and SE calculated for all samples of the corresponding folds. The right column shows the percentage error reduction for VADER compared to VAD.

spatial accuracy so that all box plots have the same y-axis. Spatial accuracy is defined as 100 % for exact hits and 0 % for a spatial deviation that corresponds to the threshold value. Generally, VADER performs better than VAD in all quantiles across all plots. It's noteworthy that, for the DGPS splits, the difference from sensor R3 to the other sensors is smaller.

For the F_1 score from the DGPS splits for a threshold value of 200 cm, the differences between VAD and VADER are still quite large. Here, the 25 % quantiles of VADER are mostly as good as or better than the 75 % quantiles of VAD (fig. 9b). With the lower threshold value of 37 cm, although the box plots overlap much more, the medians of VADER are usually above 90 %, while the medians of VAD are in the range of 50-60 % (fig. 9d). The VADER model can achieve comparable F_1 scores on the degraded sensor R3 as VAD does on the remaining sensors (fig. 9b and 9d). A similar trend is seen in the spatial accuracy (fig. 9f).

Without the sensor R3, both models show significant improvement (tab. 2). For a threshold value of 200 cm and the stratified split, VADER achieves an F_1 score of 99.4 %, reducing the error rate by 79.9 % compared to the VAD model. Just as before, VADER significantly improves the results in 31 out of 32 cases compared to its predecessor. On average for all splits and thresholds, VADER reduced the error rate by 72.84 % while also reducing the spatial error by 39.3 % for non-degraded sensors.

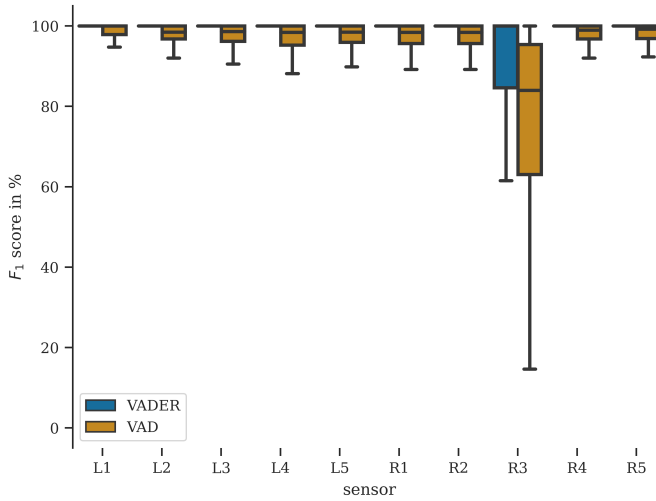
Instead of considering only the length of the train, we also examined the influence of the position of the axle within the train (fig. 10). Here, it is noticeable that the graphs for the two models and the two splits are roughly parallel to each other. VADER performs just as well or better on the more challenging **DGPS** split than VAD does on the simpler **stratified** split.

4. Conclusion

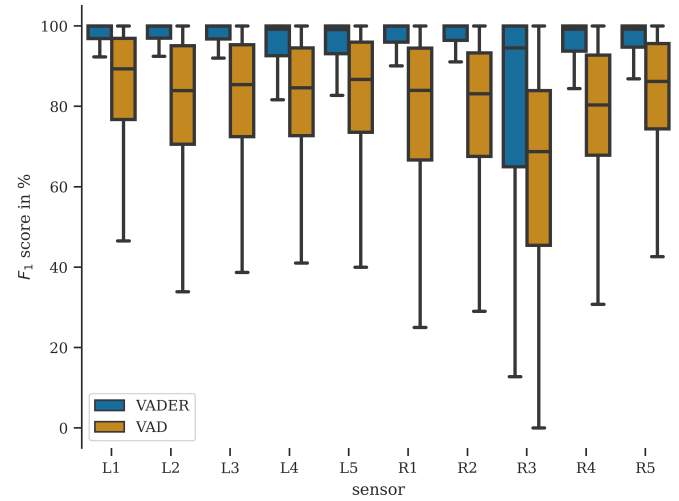
We have demonstrated that a FCN with an adequate receptive field can achieve better results using raw data compared to using a spectrogram as input. This could be due to the loss of information when transforming into spectrograms, whereas a

Threshold	Split	Metric	VAD	VADER	ER
37 cm	stratified	F_1 avg	91.5 %	98.0 %	76 %
		F_1 SD	0.26 %	0.29 %	-12 %
		SE avg	4.07 cm	2.95 cm	27 %
		SE SD	6.76 cm	5.13 cm	24 %
	DGPS	F_1 avg	57.6 %	81.5 %	56 %
		F_1 SD	1.34 %	0.45 %	66 %
		SE avg	6.96 cm	5.18 cm	26 %
		SE SD	11.0 cm	8.69 cm	21 %
200 cm	stratified	F_1 avg	97.1 %	99.4 %	80 %
		F_1 SD	0.22 %	0.06 %	74 %
		SE avg	9.46 cm	4.13 cm	56 %
		SE SD	26.9 cm	12.3 cm	54 %
	DGPS	F_1 avg	82.7 %	96.4 %	79 %
		F_1 SD	1.27 %	0.32 %	75 %
		SE avg	35.5 cm	18.6 cm	48 %
		SE SD	60.0 cm	40.3 cm	33 %

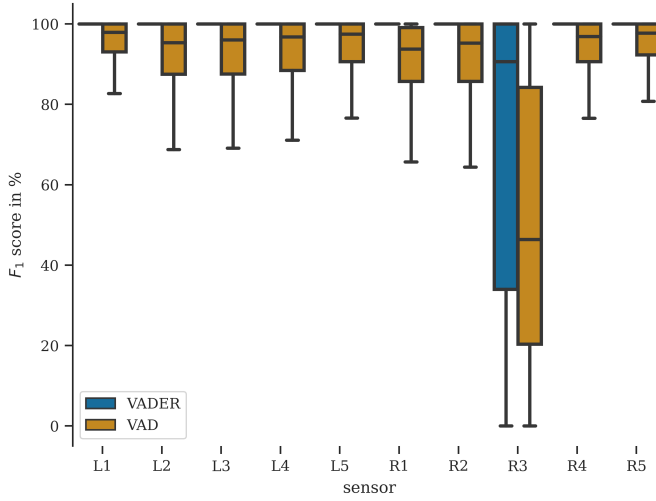
Table 2: F_1 score and SE calculated for all samples of the corresponding folds without sensor R3. The right column shows the percentage error reduction for VADER compared to VAD.



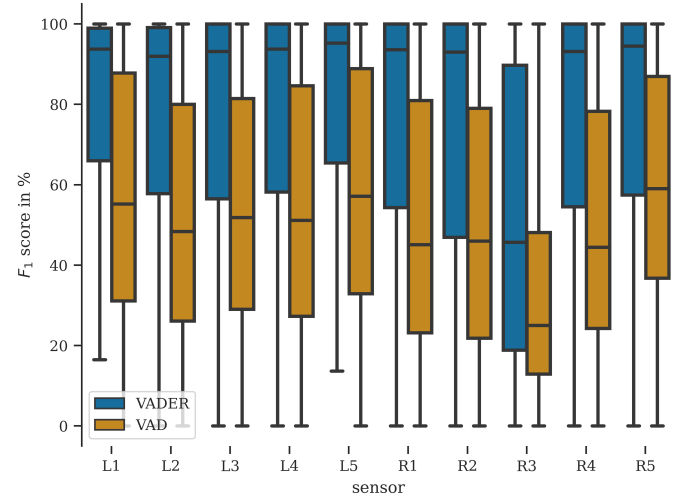
(a) F_1 score with a threshold of 200 cm for each sensor trained with the **stratified** splits.



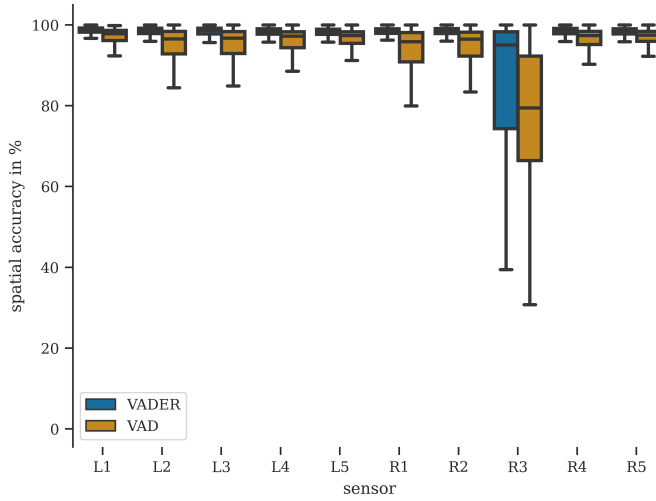
(b) F_1 score with a threshold of 200 cm for each sensor trained with the **DGPS** splits.



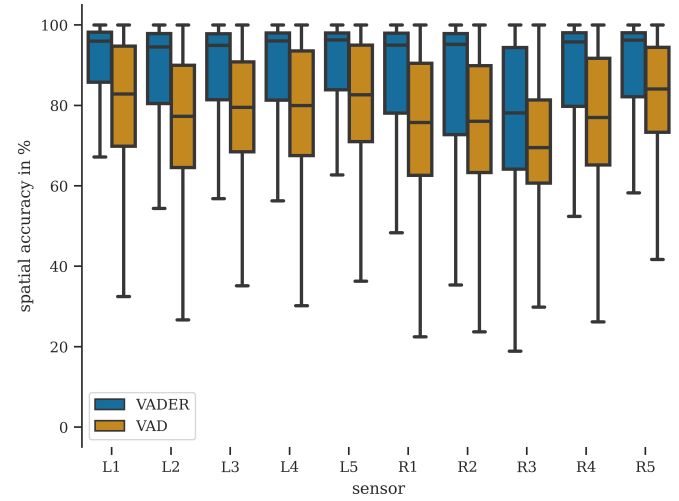
(c) F_1 score with a threshold of 37 cm for each sensor trained with the **stratified** splits.



(d) F_1 score with a threshold of 37 cm for each sensor trained with **DGPS** splits.



(e) Spatial Accuracy for a threshold of 200 cm for each sensor trained with **stratified** splits.



(f) Spatial Accuracy for a threshold of 200 cm for each sensor trained with **DGPS** splits.

Figure 9: Metrics evaluated per sensor.

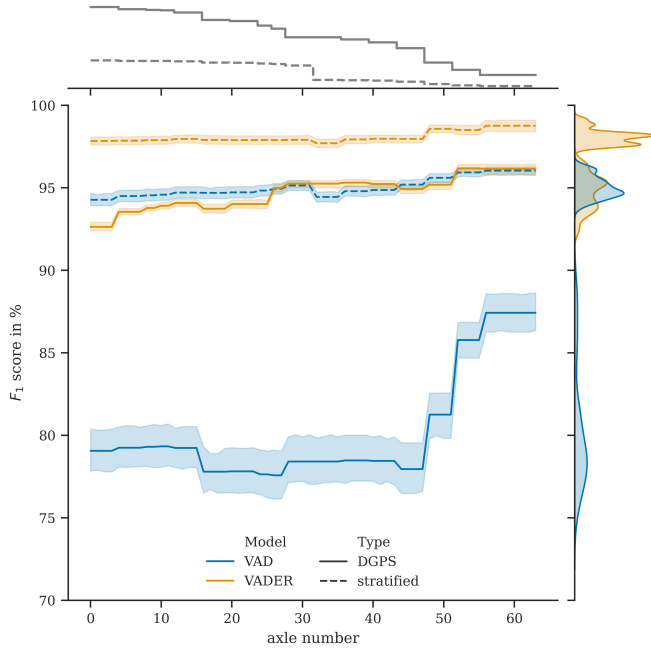


Figure 10: F_1 score in relation to the axle number in driving direction for a threshold of 200 cm. Above is a histogram of the axle numbers (shown as steps) and on the right is a kernel density plot of the F_1 scores.

FCN can directly learn to filter the data comparable to it when necessary. In order to achieve comparable or better results with raw data, we propose the RF rule to calculate the required size of the largest receptive field of a model (eq. 1). Based on our results we were already able to show the potential of raw data as input considering the RF rule.

Furthermore, we demonstrated that acceleration data is suitable for axle detection and localization. It is particularly noteworthy that even when training with only one type of train and thus a non-representative training set, we were able to achieve very good results on other train types, demonstrating that the model generalizes exceptionally well. In this case, VADER was trained solely on trains with 32 axles but could still detect 96.4 % of the axles of all other train types, with an average spatial error of 18.6 cm. Trained on a representative training set, VADER was able to detect 99.4 % of the axles with an error of just 4.13 cm. In addition to improved accuracy, VADER allows for an inference that is 65 times faster while using only 1 % of the memory. This makes the use of virtual axle detectors in real time and using edge computing possible for the first time.

With an improvement of 72.84 % in the F_1 score and 39.3 % in spatial error despite only minor model modifications, it's evident that there's significant potential yet to be unlocked. Also for VADER the signals of the acceleration sensors are evaluated individually. A joint evaluation of the signals could further increase the accuracy. Another approach could be a combination of raw input data, FCN-based spectrogram-like data transformation, and Transformer-based classification. This way, the FCN could learn how to optimally transform the data, while the Transformer model would be utilized to identify even more complex correlations and relationships.

Author Contributions

Henrik Riedel: Conceptualization, investigation, methodology, software, validation, visualization and writing - original draft. **Steven Robert Lorenzen:** Funding, supervision and writing - review & editing **Clemens Hübler:** Resources, supervision and writing - review & editing.

Acknowledgments

The research project ZEKISS (www.zekiss.de) is carried out in collaboration with the German railway company DB Netz AG, the Wölfel Engineering GmbH and the GMG Ingenieurgesellschaft mbH. It is funded by the mFund (mFund, 2020) promoted by the The Federal Ministry of Transport and Digital Infrastructure.

The research project DEEB-INFRA (www.deeb-infra.de) is carried out in collaboration with the the sub company DB Campus from the Deutschen Bahn AG, the AIT GmbH, the Revotec zt GmbH and the iSEA Tec GmbH. It is funded by the mFund (mFund, 2020) promoted by the The Federal Ministry of Transport and Digital Infrastructure.

Supported by:



on the basis of a decision
by the German Bundestag

Data and Source Code

The data [47] as well as the source code [48] used in this paper is published and contains:

1. All measurement data
2. Matlab code to label data and save as text files
3. Python code for transformation, training, evaluation and plotting.

References

[1] T. CHAN, L. YU, S. LAW, T. YUNG, Moving force identification studies, i: Theory, *Journal of Sound and Vibration* 247 (2001) 59–76. URL: <https://www.sciencedirect.com/science/article/pii/S0022460X01936302>. doi:<https://doi.org/10.1006/jsvi.2001.3630>.

[2] A. Kazemi Amiri, C. Bucher, A procedure for in situ wind load reconstruction from structural response only based on field testing data, *Journal of Wind Engineering and Industrial Aerodynamics* 167 (2017) 75–86. URL: <https://www.sciencedirect.com/science/article/pii/S0167610516303452>. doi:<https://doi.org/10.1016/j.jweia.2017.04.009>.

[3] J. Hwang, A. Kareem, W. Kim, Estimation of modal loads using structural response, *Journal of Sound and Vibration* 326 (2009) 522–539. URL: <https://www.sciencedirect.com/science/article/pii/S0022460X09004271>. doi:<https://doi.org/10.1016/j.jsv.2009.05.003>.

[4] E. Lourens, C. Papadimitriou, S. Gillijns, E. Reynders, G. De Roeck, G. Lombaert, Joint input-response estimation for structural systems based on reduced-order models and vibration data from a limited number of sensors, *Mechanical Systems and Signal Processing* 29 (2012) 310–327. URL: <https://www.sciencedirect.com/science/article/pii/S088832701200012X>. doi:<https://doi.org/10.1016/j.ymssp.2012.01.011>.

[5] A. Firus, A contribution to moving force identification in bridge dynamics, Ph.D. thesis, Technische Universität, Darmstadt, 2022. URL: <http://tuprints.ulb.tu-darmstadt.de/20293/>. doi:<https://doi.org/10.26083/tuprints-00020293>.

[6] A. Firus, R. Kemmler, H. Berthold, S. Lorenzen, J. Schneider, A time domain method for reconstruction of pedestrian induced loads on vibrating structures, *Mechanical Systems and Signal Processing* 171 (2022) 108887. URL: <https://www.sciencedirect.com/science/article/pii/S0888327022000772>. doi:<https://doi.org/10.1016/j.ymssp.2022.108887>.

[7] M. Lydon, D. Robinson, S. E. Taylor, G. Amato, E. J. O. Brien, N. Uddin, Improved axle detection for bridge weigh-in-motion systems using fiber optic sensors, *Journal of Civil Structural Health Monitoring* 7 (2017) 325–332. URL: <https://link.springer.com/article/10.1007/s13349-017-0229-4>. doi:10.1007/s13349-017-0229-4.

[8] H. Wang, Q. Zhu, J. Li, J. Mao, S. Hu, X. Zhao, Identification of moving train loads on railway bridge based on strain monitoring, *Smart Structures and Systems* 23 (2019) 263–278. URL: <https://koreascience.or.kr/article/JAK0201913457807828.page>. doi:10.12989/ss.2019.23.3.263.

[9] Y. Yu, C. Cai, L. Deng, State-of-the-art review on bridge weigh-in-motion technology, *Advances in Structural Engineering* 19 (2016) 1514–1530. URL: <http://journals.sagepub.com/doi/10.1177/1369433216655922>. doi:10.1177/1369433216655922.

[10] W. He, T. Ling, E. J. O'Brien, L. Deng, Virtual axle method for bridge weigh-in-motion systems requiring no axle detector, *Journal of Bridge Engineering* 24 (2019) 04019086. URL: [https://ascelibrary.org/doi/abs/10.1061/\(ASCE\)BE.1943-5592.0001474](https://ascelibrary.org/doi/abs/10.1061/(ASCE)BE.1943-5592.0001474). doi:10.1061/(ASCE)BE.1943-5592.0001474.

[11] E. J. O'Brien, D. Hajalizadeh, N. Uddin, D. Robinson, R. Opitz, Strategies for Axle Detection in Bridge Weigh-in-Motion Systems, in: *Proceedings of the International Conference on Weigh-In-Motion*, June, 2012, pp. 79–88. URL: https://www.researchgate.net/publication/281031765_STRATEGIES_FOR_AXLE_DETECTION_IN_BRIDGE_WEIGH-IN-MOTION_SYSTEMS.

[12] H. Zhao, C. Tan, E. J. O'Brien, N. Uddin, B. Zhang, Wavelet-based optimum identification of vehicle axles using bridge measurements, *Applied Sciences* 10 (2020). URL: <https://www.mdpi.com/2076-3417/10/21/7485>. doi:10.3390/app10217485.

[13] G. Thater, P. Chang, D. R. Schelling, C. C. Fu, Estimation of bridge static response and vehicle weights by frequency response analysis, *Canadian Journal of Civil Engineering* 25 (1998) 631–639. URL: <https://cdnsciencepub.com/doi/10.1139/197-128>. doi:10.1139/197-128.

[14] M. Zakharenko, G. T. Frøseth, A. Rönnquist, Train classification using a weigh-in-motion system and associated algorithms to determine fatigue loads, *Sensors* 22 (2022). URL: <https://www.mdpi.com/1424-8220/22/5/1772>. doi:10.3390/s22051772.

[15] M. Bernas, B. Płaczek, W. Korski, P. Loska, J. Smyła, P. Szymała, A survey and comparison of low-cost sensing technologies for road traffic monitoring, *Sensors* 18 (2018). URL: <https://www.mdpi.com/1424-8220/18/10/3243>. doi:10.3390/s18103243.

[16] G. Kouroussis, C. Caucheteur, D. Kinet, G. Alexandrou, O. Verlinden, V. Moeyaert, Review of trackside monitoring solutions: From strain gages to optical fibre sensors, *Sensors* 15 (2015) 20115–20139. URL: <https://www.mdpi.com/1424-8220/15/8/20115>. doi:10.3390/s150820115.

[17] M. Lydon, S. E. Taylor, D. Robinson, A. Mufti, E. J. O. Brien, Recent developments in bridge weigh in motion (b-wim), *Journal of Civil Structural Health Monitoring* 6 (2016) 69–81. URL: <https://link.springer.com/article/10.1007/s13349-015-0119-6>.

doi:10.1007/s13349-015-0119-6.

[18] A. Mesaros, T. Heittola, T. Virtanen, M. D. Plumley, Sound event detection: A tutorial, *IEEE Signal Processing Magazine* 38 (2021) 67–83. doi:10.1109/MSP.2021.3090678.

[19] A. Mesaros, A. Diment, B. Elizalde, T. Heittola, E. Vincent, B. Raj, T. Virtanen, Sound event detection in the dcase 2017 challenge, *IEEE/ACM Transactions on Audio, Speech, and Language Processing* 27 (2019) 992–1006. doi:10.1109/TASLP.2019.2907016.

[20] T. K. Chan, C. S. Chin, A comprehensive review of polyphonic sound event detection, *IEEE Access* 8 (2020) 103339–103373. doi:10.1109/ACCESS.2020.2999388.

[21] Y. Wang, J. Salamon, N. J. Bryan, J. Pablo Bello, Few-shot sound event detection, in: *ICASSP 2020 - 2020 IEEE International Conference on Acoustics, Speech and Signal Processing (ICASSP)*, 2020, pp. 81–85. doi:10.1109/ICASSP40776.2020.9054708.

[22] S. Latif, R. Rana, S. Khalifa, R. Jurdak, J. Qadir, B. W. Schuller, Deep representation learning in speech processing: Challenges, recent advances, and future trends, 2021. [arXiv:2001.00378](https://arxiv.org/abs/2001.00378).

[23] H. Purwins, B. Li, T. Virtanen, J. Schlüter, S.-Y. Chang, T. Sainath, Deep learning for audio signal processing, *IEEE Journal of Selected Topics in Signal Processing* 13 (2019) 206–219. doi:10.1109/JSTSP.2019.2908700.

[24] A. Radford, J. W. Kim, T. Xu, G. Brockman, C. McLeavey, I. Sutskever, Robust speech recognition via large-scale weak supervision, in: A. Krause, E. Brunskill, K. Cho, B. Engelhardt, S. Sabato, J. Scarlett (Eds.), *Proceedings of the 40th International Conference on Machine Learning*, volume 202 of *Proceedings of Machine Learning Research*, PMLR, 2023, pp. 28492–28518. URL: <https://proceedings.mlr.press/v202/radford23a.html>.

[25] S. Kiranyaz, O. Avci, O. Abdeljaber, T. Ince, M. Gabbouj, D. J. Inman, 1d convolutional neural networks and applications: A survey, *Mechanical Systems and Signal Processing* 151 (2021) 107398. URL: <https://www.sciencedirect.com/science/article/pii/S0888327020307846>. doi:<https://doi.org/10.1016/j.ymssp.2020.107398>.

[26] T. Arias-Vergara, P. Klumpp, J. C. Vasquez-Correa, E. Nöth, J. R. Orozco-Arroyave, M. Schuster, Multi-channel spectrograms for speech processing applications using deep learning methods, *Pattern Analysis and Applications* 24 (2021) 423–431. URL: <https://doi.org/10.1007/s10044-020-00921-5>. doi:10.1007/s10044-020-00921-5.

[27] B. Bozkurt, I. Germanakis, Y. Stylianou, A study of time-frequency features for cnn-based automatic heart sound classification for pathology detection, *Computers in Biology and Medicine* 100 (2018) 132–143. URL: <https://www.sciencedirect.com/science/article/pii/S0010482518301744>. doi:<https://doi.org/10.1016/j.combiomed.2018.06.026>.

[28] A. Mesaros, T. Heittola, T. Virtanen, Acoustic scene classification in dcase 2019 challenge: Closed and open set classification and data mismatch setups, in: *Workshop on Detection and Classification of Acoustic Scenes and Events*, 2019. doi:10.33682/m5kp-fa97.

[29] A. van den Oord, S. Dieleman, H. Zen, K. Simonyan, O. Vinyals, A. Graves, N. Kalchbrenner, A. Senior, K. Kavukcuoglu, Wavenet: A generative model for raw audio, 2016. [arXiv:1609.03499](https://arxiv.org/abs/1609.03499).

[30] P. Ghahremani, V. Manohar, D. Povey, S. Khudanpur, Acoustic modelling from the signal domain using cnns, in: *Interspeech 2016*, 2016, pp. 3434–3438. URL: <http://dx.doi.org/10.21437/Interspeech.2016-1495>. doi:10.21437/Interspeech.2016-1495.

[31] H. B. Sailor, H. A. Patil, Novel unsupervised auditory filterbank learning using convolutional rbm for speech recognition, *IEEE/ACM Transactions on Audio, Speech, and Language Processing* 24 (2016) 2341–2353. doi:10.1109/TASLP.2016.2607341.

[32] P. Chatterjee, E. O'Brien, Y. Li, A. González, Wavelet domain analysis for identification of vehicle axles from bridge measurements, *Computers & Structures* 84 (2006) 1792–1801. URL: <https://www.sciencedirect.com/science/article/pii/S0045794906001933>. doi:<https://doi.org/10.1016/j.compstruc.2006.04.013>.

[33] H. Kalhor, M. M. Alamdari, X. Zhu, B. Samali, S. Mustapha, Non-intrusive schemes for speed and axle identification in bridge-weigh-in-motion systems, *Measurement Science and Technology* 28 (2017) 025102. URL: <https://doi.org/10.1088/1361-6501/aa52ec>. doi:10.1088/1361-6501/aa52ec.

[34] Y. Yu, C. Cai, L. Deng, Vehicle axle identification using wavelet analysis of bridge global responses, *Journal of Vibration and Control* 23 (2017) 2830–2840. URL: <https://journals.sagepub.com/doi/10.1177/1077546315623147>. doi:10.1177/1077546315623147.

[35] Y. Zhu, H. Sekiya, T. Okatani, I. Yoshida, S. Hirano, Acceleration-based deep learning method for vehicle monitoring, *IEEE Sensors Journal* 21 (2021) 17154–17161. URL: <https://ieeexplore.ieee.org/document/9437183>. doi:10.1109/JSEN.2021.3082145.

[36] S. R. Lorenzen, H. Riedel, M. M. Rupp, L. Schmeiser, H. Berthold, A. Firus, J. Schneider, Virtual axle detector based on analysis of bridge acceleration measurements by fully convolutional network, *Sensors* 22 (2022). URL: <https://www.mdpi.com/1424-8220/22/22/8963>. doi:10.3390/s22228963.

[37] S. R. Lorenzen, H. Riedel, M. Rupp, L. Schmeiser, H. Berthold, A. Firus, J. Schneider, Virtual Axle Detector based on Analysis of Bridge Acceleration Measurements by Fully Convolutional Network, 2022. URL: <https://doi.org/10.5281/zenodo.6782319>. doi:10.5281/zenodo.6782319.

[38] A. Géron, *Hands-on Machine Learning with Scikit-Learn, Keras, and TensorFlow: Concepts, Tools, and Techniques to Build Intelligent Systems*, O'Reilly UK Ltd., Sebastopol, 2019. ISBN: 9781492032649.

[39] J. Long, E. Shelhamer, T. Darrell, Fully convolutional networks for semantic segmentation, in: *2015 IEEE Conference on Computer Vision and Pattern Recognition (CVPR)*, 2015, pp. 3431–3440. URL: <https://doi.org/10.1109/CVPR.2015.7298952>.

//ieeexplore.ieee.org/document/7298965. doi:10.1109/CVPR.
2015.7298965.

[40] O. Ronneberger, P. Fischer, T. Brox, U-net: Convolutional networks for biomedical image segmentation, in: Medical Image Computing and Computer-Assisted Intervention – MICCAI 2015, Springer International Publishing, Cham, 2015, pp. 234–241. URL: https://link.springer.com/chapter/10.1007/978-3-319-24574-4_28. doi:10.1007/978-3-319-24574-4_28.

[41] K. He, X. Zhang, S. Ren, J. Sun, Deep residual learning for image recognition, in: 2016 IEEE Conference on Computer Vision and Pattern Recognition (CVPR), 2016, pp. 770–778. URL: <https://ieeexplore.ieee.org/document/7780459>. doi:<https://doi.org/10.1109/CVPR.2016.90>.

[42] S. Ioffe, C. Szegedy, Batch normalization: Accelerating deep network training by reducing internal covariate shift, in: Proceedings of the 32nd International Conference on International Conference on Machine Learning - Volume 37, ICML'15, JMLR.org, 2015, p. 448–456. URL: <https://proceedings.mlr.press/v37/ioffe15.html>.

[43] Y. Wu, K. He, Group normalization, International Journal of Computer Vision 128 (2020) 742–755. URL: <https://doi.org/10.1007/s11263-019-01198-w>. doi:10.1007/s11263-019-01198-w.

[44] M. Abadi, A. Agarwal, P. Barham, E. Brevdo, Z. Chen, C. Citro, G. S. Corrado, A. Davis, J. Dean, M. Devin, S. Ghemawat, I. Goodfellow, A. Harp, G. Irving, M. Isard, Y. Jia, R. Jozefowicz, L. Kaiser, M. Kudlur, J. Levenberg, D. Mané, R. Monga, S. Moore, D. Murray, C. Olah, M. Schuster, J. Shlens, B. Steiner, I. Sutskever, K. Talwar, P. Tucker, V. Vanhoucke, V. Vasudevan, F. Viégas, O. Vinyals, P. Warden, M. Wattenberg, M. Wicke, Y. Yu, X. Zheng, TensorFlow: Large-scale machine learning on heterogeneous systems, 2015. URL: <https://www.tensorflow.org/>, Accessed: 11.08.2021.

[45] H. Iqbal, Harisiqbal88/plotneuralnet v1.0.0, 2018. URL: <https://doi.org/10.5281/zenodo.2526396>. doi:10.5281/zenodo.2526396.

[46] D. P. Kingma, J. Ba, Adam: A method for stochastic optimization, 2017. [arXiv:1412.6980](https://arxiv.org/abs/1412.6980).

[47] S. R. Lorenzen, H. Riedel, M. Rupp, L. Schmeiser, H. Berthold, A. Firus, J. Schneider, Virtual Axle Detector based on Analysis of Bridge Acceleration Measurements by Fully Convolutional Network, 2022. URL: <https://doi.org/10.5281/zenodo.6782319>. doi:10.5281/zenodo.6782319.

[48] H. Riedel, hjhriedel/vader: v0.2-alpha, 2023. URL: <https://doi.org/10.5281/zenodo.8296526>. doi:10.5281/zenodo.8296526.